Stroboscopic Ultrafast Imaging Capabilities Using RF Strip-lines in a Commercial Transmission Electron Microscope

Spencer A. Reisbick[1], Myung-Geun Han[1], Chuhang Liu[1,2], Yubin Zhao[3], Eric Montgomery[3], Chunguang Jing[3], Vikrant J. Gokhale[4], Jason J. Gorman[5], June W. Lau[6] and Yimei Zhu[1,*]

[1]*Condensed Matter Physics and Materials Science Department, Brookhaven National Laboratory, Upton, NY 11973, USA*

[2]*Department of Physics and Astronomy, Stony Brook University, Stony Brook, NY 11794, USA*

[3]*Euclid Techlabs LLC, 365 Remington Blvd. Bolingbrook, IL 60440, USA*

[4]*Microsystems and Nanotechnology Division, National Institute of Standards and Technology, Gaithersburg, MD 20899, USA.*

[5]*U.S. Naval Research Laboratory, Washington, DC,20003 USA*

[6]*Materials Science and Engineering Division, National Institute of Standards and Technology, Gaithersburg, MD 20899, USA.*

Abstract: The development of ultrafast electron microscopy (UEM), specifically stroboscopic imaging, has brought the study of structural dynamics to a new level by overcoming the spatial limitations of ultrafast spectroscopy and the temporal restrictions of traditional TEM simultaneously. Combining the concepts governing both techniques has enabled direct visualization of dynamics with spatiotemporal resolutions in the picosecond-nanometer regime. Here, we push the limits of imaging using a pulsed electron beam *via* RF induced transverse deflection based on the newly developed 200 keV frequency-tunable strip-line pulser. We demonstrate 0.2 nm spatial resolution at high magnifications and elucidation of Lorentz imaging using the phase-microscopy method. We also present beam coherence measurements and expand our study using the breathing modes of a silicon interdigitated comb under RF excitation which achieves improved temporal synchronization between the electron pulse-train and electric field. A new RF holder has also been developed with impedance matching to the RF signal to minimize transmission power loss to samples and its performance is compared with a conventional sample holder.

Keywords: Ultrafast electron microscopy, electron pulser, frequency-tunable RF excitation, time-resolved stroboscopic imaging, coherent electron pulses.

1. INTRODUCTION

Atomic imaging *via* transmission electron microscopy (TEM) has become a powerful characterization technique due to aberration correction and direct electron detection [1–4]. The technique is widely used for materials characterization because of its ability to elucidate crystallographic and compositional structures of single-particles [5–8]. Traditionally, the electron beam is continuous with a pseudo-random emission profile on the specimen. As a result, typical temporal resolutions of conventional electron microscopy are limited to a few milliseconds due to the frame rate of the detector [9–11]. These domains enable dynamic observation of slow *in situ* processes such as Avrami crystallization and biological degradation [12–14]. However, complex magnetic and electronic dynamics can occur in the sub-picosecond regime [15–18].

Ultrafast electron microscopy (UEM) has been developed to elucidate nanometer scale structural dynamics occurring in their native temporal domains. Quantum information sciences poses some of the most promising UEM applications because of its unique ability to image in an exclusive spatiotemporal domain. Specifically, qubit devices and emerging spintronic devices can transmit data at operation frequencies up to 10 GHz which typically exceed the temporal visualization requirements in most current UEM systems [19–21]. Alternative mechanisms for data transmission are also emerging although the fundamental processes are not completely understood [22,23]. The development of UEM enables the exploration of processes occurring at femtosecond temporal and nanometer spatial scales simultaneously [24–26]. Operation is

predicated on a pseudo-binary distribution of electron-specimen interactions through beam blanking or laser illumination [27]. Laser-based techniques are the most frequent form of electron pulse generation in UEM because of the resemblance to ultrafast spectroscopy. However, inhibitors of femtosecond lasers include cost, placement and the excitation frequency range (typically up to a few MHz). More importantly, laser induced thermal heating and the difference in penetration depth between the photon-pump and electron-probe at the sample has encouraged alternative methods to electron pulse generation [28,29]. Figure 1 contains a schematic of the Euclid Techlabs' UltraFast Pulser[i] (hereafter referred to as the pulser), which is an alternative to laser-based UEM [30–32]. The electron beam enters an RF strip-line (K1) which sweeps it laterally across a beam chopping aperture (BCA). Short electron pulses transmit through the aperture with a large momentum distribution, then enter a second RF strip-line (K2) designed to demodulate the momenta dispersion to the original state. Fractional amounts of electrons transmit through the BCA forming pulses as small as 10 ps that are tunable *via* the sweeping frequency, BCA diameter and applied voltage across K1 [30–32]. Placing the pulser downstream from the gun chamber retains the original emission making it the largest advantage of RF strip-line technology in UEM. Without additional lasers, conventional TEM modalities are recovered by removing the applied potential across both strip-lines and retracting the BCA.

Here, we demonstrate quantitative comparisons between continuous and pulsed electron beams *via* the pulser installed on the JEM 2100F electron microscope[i]. We evaluate a myriad of common electron microscopy techniques and their quantitative ability to retain contrast features. The microscope has been modified from previous work by replacing its original field-free polepiece with a high-resolution polepiece to improve spatial resolution [30–32]. Additionally, we have implemented a new alignment technique between K1 and K2 with additional grounding

to prevent charging. As a result, we resolve 0.2 nm lattice fringes and elucidate phase images of magnetic domains for the first time using electron pulses as small as 10 ps [33–36]. Further, we find anisotropic retention of the coherence through classic Fresnel fringe measurements that aligns directionally with the sweeping motion of the electron beam [37]. We also demonstrate a new RF compatible holder with improved power transmission and explore the intricate imaging conditions and optimization of an interdigitated silicon comb for time-resolved experiments [30–32].

2. MATERIALS AND METHODS

2.1 Electron Microscopy Data Acquisitions

Electron micrographs were acquired using a JEOL JEM-2100F TEM operated at 200 kV with the pulser inserted directly below the field-emission electron gun. Explanation of physical connections and general operation can be found elsewhere [30–32]. The relevant aperture sizes, RF sweeping frequency and K1/K2 modulation and demodulation parameters for all images are provided in Table S1. Specifically, most images were acquired using a 2.6 GHz sweeping frequency and 0.3 V K1 sweeping voltage (noted if other). Note that the corresponding frequency of electron packet arrival at the sample is doubled to 5.2 GHz due to the forward and back motion through the pulser. The resulting pulse duration at these conditions was measured to be about 30 ps; however, increases in frequency or K1 voltage are accessible options to reduce the temporal width of the electron packets further. Images were acquired using a Gatan UltraScan 1000XP 4-megapixel camera. A LabVIEW control interface was used to control the applied voltages and phase applied to K1 and K2. All specimens, except for the evaporated permalloy (Py) film, were calibration standards.

2.2 Evaporated Permalloy Sample Preparation

A Py film was evaporated over a 2000 mesh copper grid onto a 100 μm x 100 μm x 10 nm silicon nitride (SiN) window while taped to an aluminum foil platform in a home-built film evaporator. The electron gun was run at 80 μA until the sample reached an approximate thickness of 20 nm. The 2000 mesh copper grid was removed leaving the SiN window with Py squares nearly 6.5 μm x 6.5 μm in size with a 4 μm lateral separation.

2.3 Holder Transmission Measurements

Power transmission through the RF compatible TEM holder was measured *via* the S_{21} transmission signal using a network analyzer. The signal was passed from the network analyzer to the holder without a sample to measure only the losses of the holder. A high frequency probe was connected to the signal line on a custom printed circuit board (PCB) carrier.

3. RESULTS AND DISCUSSION

3.1 Installation comparison of the ultrafast pulser

Recent advancements in UEM have enabled direct visualization of materials responses on their native time scales [38–47]. The pulser can quickly change its operation mode between a continuous and pulsed electron beam with minimal tuning of the microscope optics. Three primary modifications to the microscope and pulser have improved the imaging capabilities. The alignment procedure between K1 and K2 has been improved such that the center of the pulser is easier to align along the optic axis of the microscope. Lead shielding around the deflection cavity has also been employed to prevent charging from electrons scattering off the BCA. Lastly, we have inserted a 2.3 Å point-to-point high-resolution pole piece to improve the spatial resolution.

Figure 1 contains a schematic of the components used to modulate and demodulate the beam to pulse the electron beam. After exiting the gun assembly, the electron beam enters K1 and is laterally swept across the BCA, chopping it into pulses with picosecond duration that enter K2. K2 demodulates the electron pulses with an RF field 180° out-of-phase from K1 before transmitting them to the traditional lens system of the TEM. Figure 1c demonstrates the quality of the electron beam in continuous and pulsed operation. Each measured parameter was extracted by fitting the beam profile to an error function (See Figure S1). The pulser increases the distance between the electron cathode and condenser aperture by about 0.5 m, so we have checked the retention of electron counts before and after installation (Figure 1d). The maximum beam currents were not compromised due to the installation of the pulser at the sample and subsequent detectors when the microscope is used conventionally. More information regarding the methodology and specific measurements can be found in Figure S1.

Figure 1. Illustration of the pulser installation on a JEOL JEM-2100F TEM. (a) Schematic of a traditional TEM with the pulser inserted below the cathode as indicated by the red box. (b) Magnified and exaggerated rendering of the pulser components used for modulation (K1) and demodulation (K2) of the electron beam. The electron beam is swept by K1 over a BCA to generate pulses. Electron pulses drift with dispersed momenta directions, so K2 demodulates them through a time-dependent RF field, locked at 180° with respect to K1. (c) Comparison of the electron beam in continuous and pulsed operation using the fitting parameters to an error function (see Figure S1). The width and intensity refer to the diameter and number of electrons in the beam, respectively. The blurriness of the beam edge was measured using the FWHM. The inset contains

micrographs of the continuous (left) and pulsed (right) beams for comparison. Error bars are the standard deviation of triplicate measurements for each fit parameter. (d) Comparison of the electron beam intensity at different magnifications before and after pulser installation using an illumination about 5 cm. Quantitative comparisons are only to demonstrate that analogous beam currents are achievable with the pulser modification. Error bars are the standard deviation of triplicate measurements over different days before and after installation.

Two of the most important capabilities of the pulser is the quality of the pulsed electron beam and retention of conventional TEM performance. Upon activation of the sweeping mechanisms in K1 and K2, the width of the beam is not affected, indicating that demodulation is effective. However, the intensity in the electron beam drops by 75-90% depending on the RF voltage and sweeping frequency (duty cycle) applied to K1. Reducing the BCA diameter produces shorter electron pulses, but loses signal, requiring a compromise between temporal duration and image intensity. Modulation of the electron beam induces a transverse broadening of the electron beam which is mostly corrected using K2 as shown by the full width at half-maximum (FWHM) of the intensity rise of the beam. When the beam is continuous, edges are sharper because the electron beam is not being modified. The pulser intentionally moves the electron beam off-axis and compensates for most of the modulation, but still contains a slight distortion. The beam currents are comparable before and after installation when the pulser electronics remain off. The quantity of electrons reaching the detector is maintained regardless of the additional 0.5 m drift space between the exit of the gun chamber and first condenser lens. Note that previous publications using the pulser were based on a low-excitation, magnetic field free objective lens pole piece rather than the high-resolution pole piece used here [30–32]. Specifically, this pole

piece has a 0.23 nm point to point resolution and a tilt range ±40° and ±30° for the α and β directions, respectively. The work presented here examines techniques including Fresnel and high-resolution imaging in addition to traditional bright field and diffraction. After installation of the high-resolution pole piece, the gun and lens operating conditions were optimized, so quantitative comparison of the beam currents is not as important as the ability to maintain prior electron quantities for imaging.

3.2 Standard imaging capabilities using the ultrafast pulser

The most common imaging techniques in traditional TEM for materials characterization purposes are bright field imaging and diffraction. We imaged gold nanoparticles deposited on holey carbon film as shown in Figures 2a and 2b with continuous and pulsed beams, respectively. We have intentionally induced vertical astigmatism in the images to quantitatively compare distortions in the imaging conditions. Figure 2c contains the respective diffraction patterns (DP) of the gold nanoparticles where the contrast of the pulsed electron beam has been enhanced to demonstrate that six diffraction rings are visible in both operation modes. Figures 2d, 2e and 2f provide quantitative comparisons of the bright field and diffraction images using the pulser. In bright field imaging, the intensity, contrast and sharpness correspond to the total electrons, local gradient of the intensity and width of the gradient (See Figure S2), respectively. In diffraction, the spacing and width were measured by fitting the radially averaged (220)-peak (1.43 Å) to a Gaussian (See Figure S2). The (220) peak was selected for fitting purposes because it is spatially isolated, even though higher order planes are visible. Radial integration of the diffraction patterns is provided in Figure 2e with each set of planes labeled. Note that there is a large disparity between

the intensity of the continuous and pulsed electron beams, so each integration has been normalized and offset to demonstrate the shape.

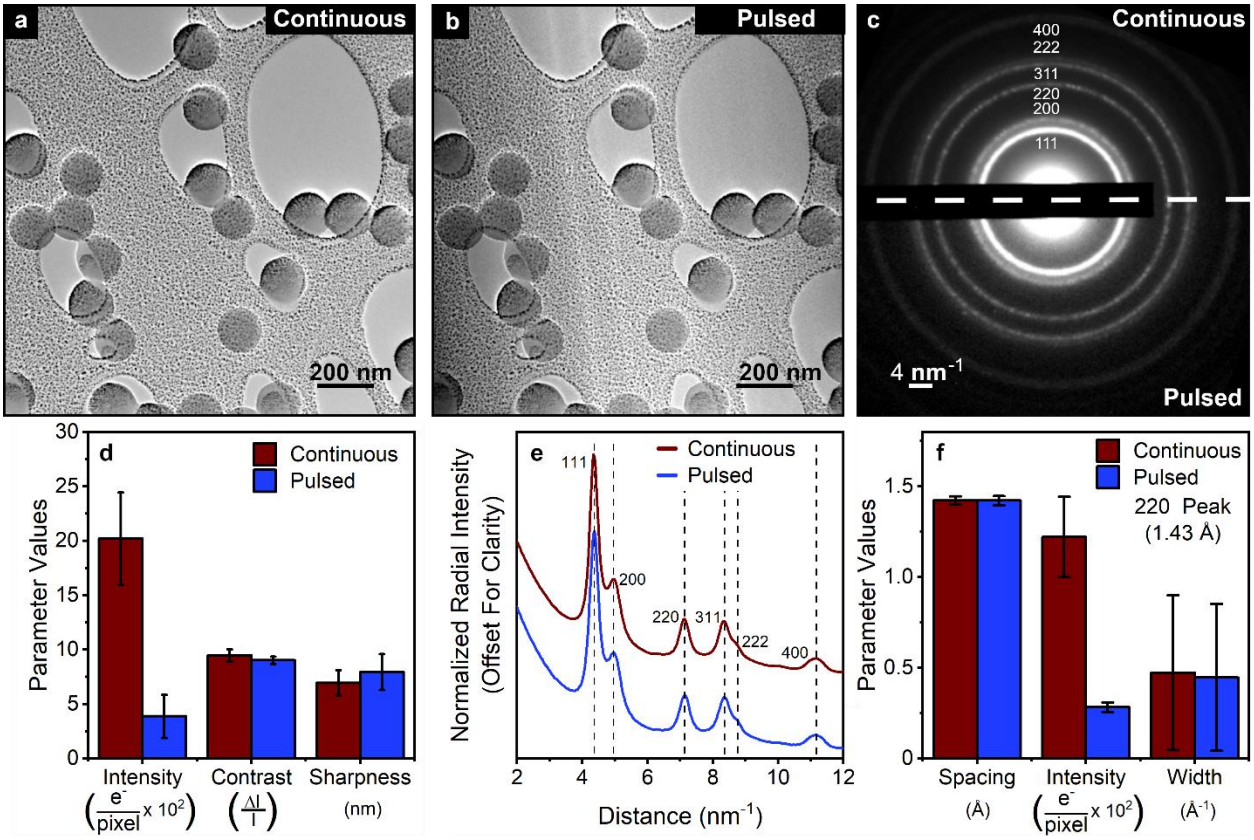

Figure 2. Demonstration of bright field and diffraction capabilities using the pulser. (a, b) Bright field images of gold nanoparticles on holey carbon using continuous (a) and pulsed (b) electron beams with 5 s same acquisition times. (c) Diffraction patterns from (a) and (b) with the planar reflections for gold indicated for a continuous (top) and pulsed (bottom) electron beam. (d) Quantitative comparison of the bright field images in (a) and (b). Intensity refers to the average number of electrons collected such that the ratio between the two is equal to the duty cycle of the pulsed beam (~20%). Contrast and sharpness refer to the intensity magnitude change and width along intentionally bright astigmatic boundaries (see Figure S2). Error bars are the standard deviation of triplicate measurements at different sample locations. (e) Normalized radial

integrations of the DP intensity profile in (c). Note the intensity disparity is nearly five-fold, so the vertical axis has been normalized to demonstrate the curve shape rather than the amplitude. (f) Quantitative comparison of the (220)-peak for each radially integrated intensity profile. The d-spacing, intensity and width refer to the position, amplitude and FWHM of a Gaussian fit. Error bars are the standard error for each fitting parameter.

Image differences in bright field and diffraction are qualitatively undetectable between continuous or pulsed operation of the pulser. The main difference is the reduction of electron counts due to the removal of many off-axis electrons by the BCA. This can be corrected by longer acquisition times but requires increased stability of the probe and specimen. Quantitatively, the resolution, contrast, and position of features are all retained within statistical error. The most important aspect in imaging with the new pulser system is that the images are not altered by the imposed sweeping motion of the RF field. Here, we verify that the modulation of the electron beam is sufficiently corrected to retain the original images and corresponding quantitative information. The intensity is reduced by nearly 80% during pulsed operation, so acquisitions require five times longer to achieve similar counts. Specimen stability at very low magnifications is typically not an issue, so decreasing the K1 sweeping voltage or increasing the RF frequency is an alternative to increase the quantity of electrons reaching the sample. Increases in the BCA diameter also allows increased electron transmission at the cost of a higher duty cycle. Consequently, each of these adjustments increase the pulse duration which becomes important for time-resolved dynamic analysis.

To test the magnetic imaging capabilities of the pulser we used Lorentz phase transmission electron microscopy (LTEM) *via* Fresnel contrast [35]. In phase microscopy, magnetic moments

in the sample deflect transmitted electrons when the beam is not at focus. The deflection angle and subsequent amplitude increases as the magnitude of defocus is increased. Spin-induced deflection of incident electrons is equivalent to the change of phase of the electron wavefront in a quantum mechanical description. In Figure 3, we present magnetic vortex states in evaporated 6.5 μm Py squares with the corresponding difference, phase and induction maps for continuous and pulsed electron beams [48,49]. Over- and under-focused images were acquired 3.1 mm away from eucentric focus. The phase of the square element was retrieved using the transport-of-intensity (TIE) method through standard reconstruction procedures [50–52]. We note sufficient stability to detect ripple contrast in the polycrystalline Py elements due to its magnetocrystalline anisotropy. Line profiles of the vortex-cores and the subsequent Gaussian fits (Figure S3) suggest there is no difference in spatial resolution of the Lorentz imaging using continuous and pulsed beams. The phase and corresponding induction maps correspond demonstrate the reconstructed magnetic spin directions in the Py sample.

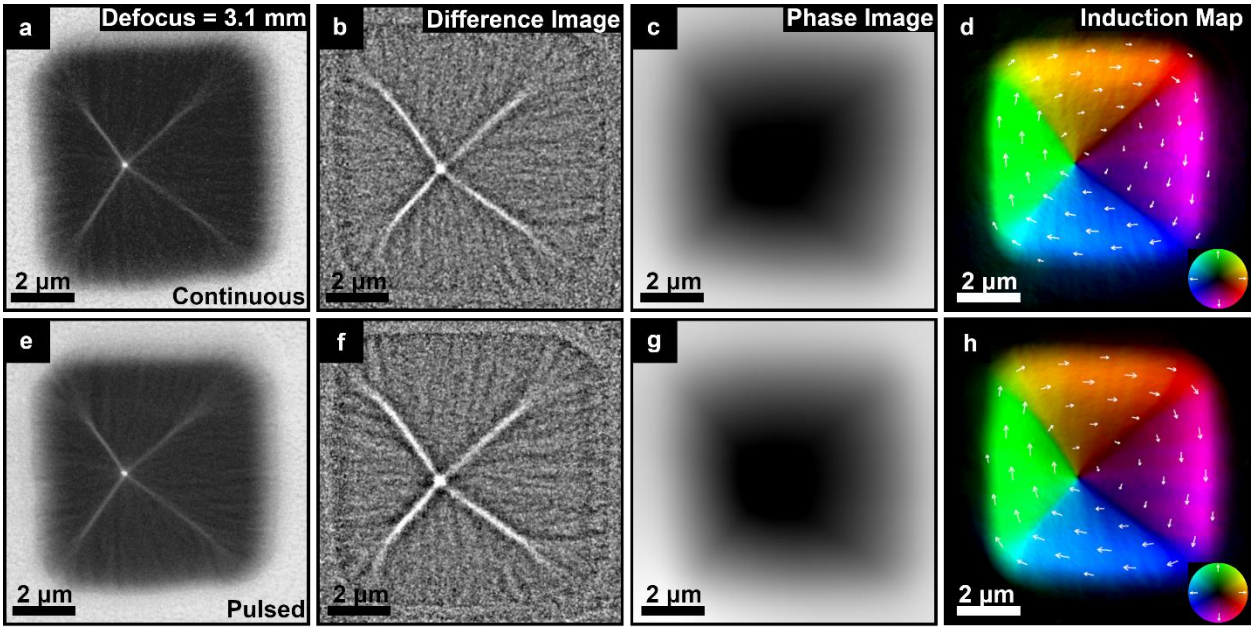

Figure 3. Demonstration of LTEM using a 6.5 μm Py square during operation of the electron pulser. (a, e) Py square imaged using continuous (a) and pulsed (e) electron beams at a defocus of 3.1 mm. Images are adjusted to similarly represent the intensity. (b, f) Difference between over- and under-focused images after alignment. (c, g) Phase images constructed from the alignment of over- and under- focused LTEM images. (d, h) Induction maps, or vector maps, based on TIE analysis showing the reconstructed spin arrangement. The color and brightness correspond to the in-plane spin direction and amplitude, respectively (see color-wheel legend at the right-bottom corner). The spin directions are also shown as arrows overlayed on the color map. Quantitative comparisons in the same format of the other figures in this paper are provided in the Supplementary Information.

Since LTEM requires a defocused electron beam to detect the phase of the electron wave front passing through a sample, a Py square with the magnetic Landau structure (vortex core with four 90° domain walls) was used to test whether the pulser would be able to retain electron phase information qualitatively and quantitatively. Qualitatively, spin reconstructions using the TIE retrieval method show minimal differences in retrieval of the magnetic signals. Quantitative analysis confirms that the primary difference in operation lies in the intensity of the acquisition and the necessary collection times. The 80% intensity reduction agrees with bright field imaging for similar K1 voltages and chopping apertures. Furthermore, the sharpness of the vortex center using a pulsed beam now lies within statistical error of the continuous beam. The presence of magnetic domains amplifies the effects of modulated electrons, meaning significant improvements in demodulation can be achieved using phase imaging techniques. Recall that the K1 sweeping motion induces two electron packets of unique momenta *via* the forward and backward

propagation across the chopping aperture. Improper demodulation manifests as double images due to the inverse momentum vectors and is amplified when the beam is defocused. The dispersion amplification acts to assist in more precise demodulation because of the oppositely dispersed electron packets.

At low magnifications, the continuous and pulsed electron beams yield almost no differences when imaging the sample because the alignments are not as sensitive to demodulation. Ideally, pulsed electron beams with would retain the best achievable spatial resolution compared to the continuous counterpart. However, the field has struggled to simultaneously retain the spatial resolution of traditional TEM when the pulse duration is reduced below the nanosecond regime [53]. Figure 4 contains images using tens of picosecond electron pulses to resolve 0.2 nm lattice fringes (corresponding to the 200 reflection) in gold nanoparticles using a 0.23 nm point-to-point high-resolution pole-piece. Specifically, we resolve multiple domains within a single nanoparticle as shown in Figure 4b. It should be noted that switching between continuous and pulsed operation at high magnifications requires different lens alignments. As well, the objective and condenser lens astigmatism alignments require additional tuning due to the elongation of the electron beam in K1. To correct for imperfections in demodulation, intentional astigmatism was introduced to correct a spherical aberration caused by the sweeping motion. The insets of Figure 4 contain a comparison of the FFT spectra when using continuous and pulsed electron beams to demonstrate the quantitative consistency between high resolution images. Further, Figure 4f quantitively compares the contrast, d-spacing and total dose for each acquisition. Note that the pulsed acquisition has been lengthened to approximately match the total quantity of electrons arriving at the sample (~450 e^- per pixel).

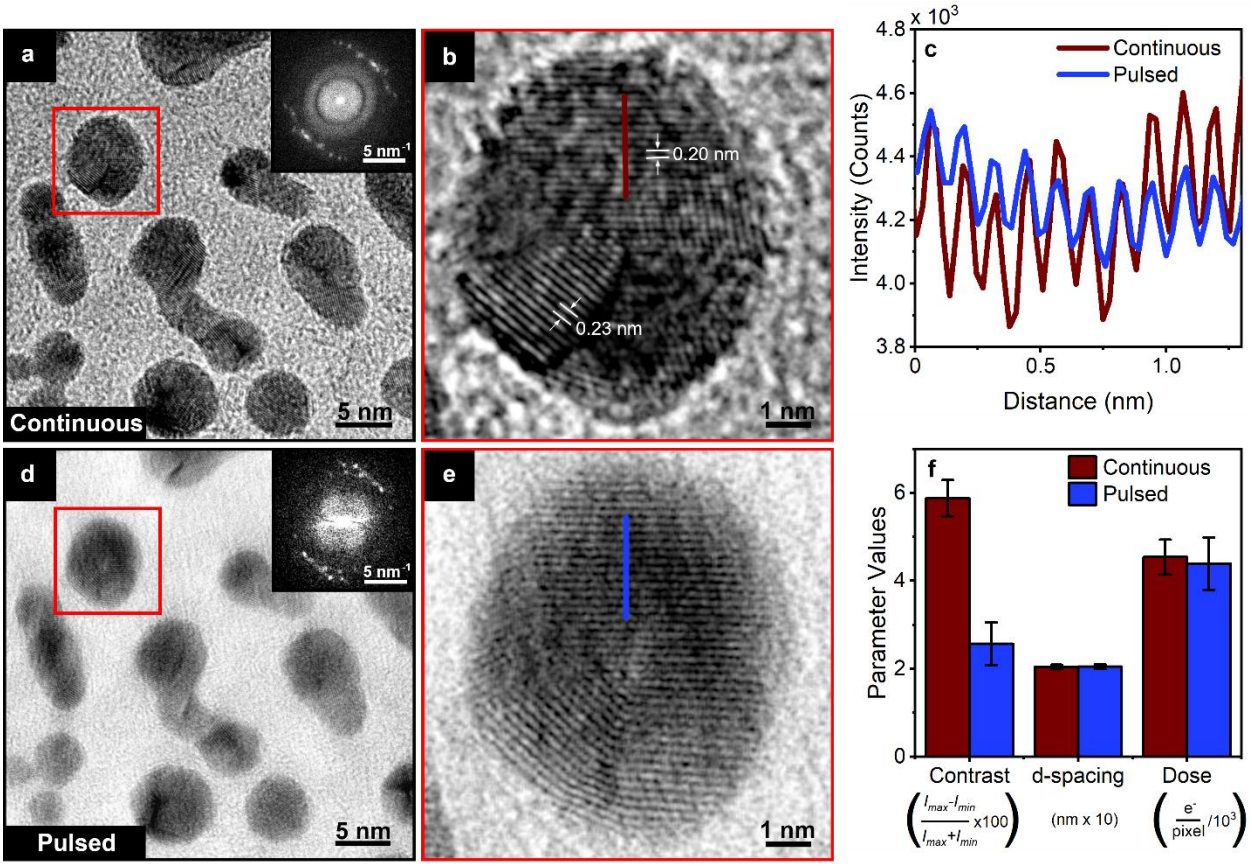

Figure 4. High-resolution imaging of gold nanoparticles using continuous and pulsed electron beams. (a, d) Bright field images of gold nanoparticles using continuous (a) and pulsed (d) electron beams without an objective aperture. Images were acquired using a 0.15 V K1 kicking voltage and 3 GHz sweeping frequency (pulse duration of 60 ps) to increase the total number of electron counts. (b, e) Magnified images from the regions-of-interest in (a) and (d). Pulsed beam images were acquired longer to achieve similar total doses to ensure that fringe visibility was not affected by signal reduction. (c) Intensity line profiles taken from (b) and (e) along the respective ROIs. (f) Quantitative comparison of the contrast, lattice spacing and accumulated dose using the continuous (maroon) and pulsed (blue) electron beams measured from the line profiles in (c). Error bars is the standard error of values extracted from the line profiles in (c).

At higher magnifications, the differences between the continuous and pulsed electron beams are more apparent, primarily due to the disparity in electron counts. However, the magnitude of the FFT peaks and corresponding lattice spacing are unaltered when imaged with the pulsed electron beam. We have noticed that the sensitivity of lattices spacings oriented relative to the sweeping direction of the beam are correlated. Currently, any deviation between the alignment of crystallographic planes and electron beam motion causes anisotropic resolution reduction and requires additional tuning of the electron beam. We believe that additional tuning the internal alignments of the pulser will further enhance the spatial resolution. Secondly, similar electron counts for the pulsed beam image required a longer acquisition and more converged beam, causing additional aberrations in the image. We have implemented both techniques to achieve similar dose quantities in the continuous and pulsed images to prevent time-dependent specimen drift. Due to the balance between acquisition time and sufficient SNR there are still improvements that are being implemented to the pulser but have provided evidence of the substantial improvement.

3.3 Modulated pulsed electron beam coherence using the ultrafast pulser

We further evaluate the beam coherence and its importance for phase imaging such as Lorentz microscopy and holography as tools for quantum information science. Here, we demonstrate anisotropic retention of the electron beam coherence by imaging Fresnel fringes from a 5 μm hole in a SiN substrate [54]. Because the hole is round, we can evaluate the coherence with a 360° angular distribution relative to the beam sweeping direction. Figure 5 contains the respective Fresnel fringes for a continuous and pulsed electron beam with two orthogonal directions indicated. Figures 5c and 5f contain line profiles parallel (1) to and perpendicular (2) the beam sweeping direction as a comparison of the anisotropy. Here, the quantity of fringes

directly corresponds to the translational coherence of the beam and the effective size of the initial source [55,56].

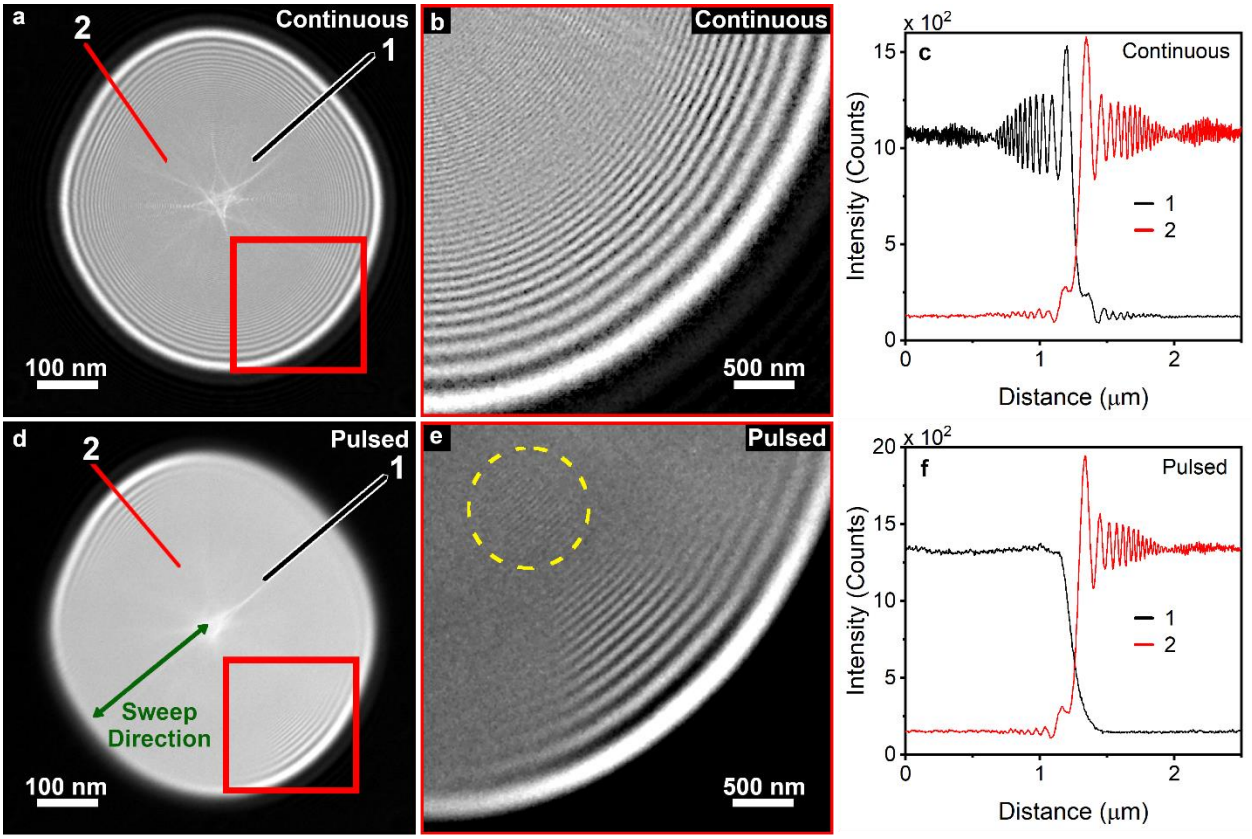

Figure 5. Anisotropic electronic beam coherence using the RF pulser on a round SiN window. (a, d) Defocused image (-11 mm) image of a round SiN window acquired using a continuous (a) and pulsed (d) electron beam. Pulsed beam images were acquired with a 0.2 V K1 kicking voltage (pulse duration of 40 ps) to increase the intensity of the images. The directions parallel (1) and perpendicular (2) to the beam sweep direction (green arrow) have been indicated. Note that the accumulated acquisition time for the continuous and pulsed images are 20 and 90 seconds, respectively, causing the latter to appear brighter (duty cycle of 40%). (b, e) Magnified images from the ROIs in (a) and (d) to enhance the quantity of visible Fresnel fringes. The brightness and contrast in (e) have been modified to amplify the appearance of the fringes at the cost of other features. The yellow circle contains higher order Fresnel fringes during the pulsed acquisition

which are oriented parallel to the beam sweeping direction. (c, f) Anisotropic line profiles laying parallel (black) and perpendicular (red) to the beam sweeping direction showing the coherence during continuous (c) and pulsed (f) operation.

During pulsed operation, the Fresnel fringes at the edges of the SiN window parallel to the sweeping direction of the electron beam retain their visibility more than those perpendicular. In fact, fringes aligned perpendicular to the beam sweeping direction are almost entirely unresolvable. In Figure 5d, the translational coherence is isotropic during continuous beam operation with fringes reaching the spatial limitations of the camera. Note that the quantity and clarity of the fringes do not change with respect to the angular component from the center of the SiN hole. Changing to a pulsed electron beam reduces the coherence anisotropically due to the modulation of the electron beam along one direction. Consequently, the parallel and perpendicular translational coherences relative to the beam sweeping direction is reduced and maintained, respectively. Ideally, demodulation would return the electron pulses back to the original size and momentum of the continuous beam, so there is room for improvement in this evaluation. The translational coherence of the electron beam is radially dependent on the beam sweep direction, so it is promising that directional phase methods (*i.e.* Holography) can be accomplished using this quality. Further, smaller chopping apertures (currently limited to 25 μm) would reduce the momenta distribution of the electron beam exiting K1, which would simplify in K2 demodulation and potentially improve the data quality.

3.4 Development of a new RF compatible holder for use with the ultrafast pulser

One purpose of developing an electron pulser is to conduct laser free ultrafast experiments under RF excitation with potential to provide direct observations of qubit or high-speed devices at 4K in operando. Among the challenges we are facing, the sample holder must be compatible with the RF transmission signal and have minimal power losses. We have developed a new sample holder (Figure 6a) that is impedance matched to yield improved signal transmission to the sample by introducing a vacuum compatible RF transmission line capable of operating at frequencies greater than 0.5 GHz. In previous experiments, we examined RF driven electrostatic breathing modes in silicon comb structures shown in Figure 6c [30–32]. Tuning the relative delay between the RF excitation through the comb structure and the electron pulse propagation allowed direct visualization of electron deflection due to the periodic potential surrounding the comb structure. However, the maximum transmission (above 0.5 GHz) was near 40%, then dropped below 5% at 3.5 GHz [30–32]. The RF input is connected *via* an SMA connection located on the rear of the holder. This signal line travels down the center of the holder architecture and exits as a wire near the normal position of the sample. We have also designed interchangeable PCB chip carriers that are easily inserted into contact with the signal line through a screw-based clamping mechanism (See supplementary information). In Figure 6a, the PCB has signal and ground lines passing through the center and edges of the board, respectively. The sample is mounted in a standard 3 mm opening that splits the signal line. Bonding is required to electrically connect the sample to the signal line on the PCB carrier chip. To test the holder, we replicated electrostatic breathing modes in an interdigitated comb using an RF input power of 0.5 W (comparable to previous magnitudes) and excitation frequency of 5.2 GHz [31]. We previously did not discuss the effect of defocus on breathing modes in the interdigitated comb structure. Electrostatic breathing modes

are amplified using a largely under- or over-focused electron beam. However, focusing electron beam does not deflect the electrons enough to measure any modulation in the tine widths.

Figure 6. Development of a low-loss stroboscopic TEM holder for RF excitation. (a) Schematic and image of the RF compatible holder using a PCB chip carrier as the sample mounting substrate. A thorough description of the holder is available in the supplementary information. (b) Electrical connections between the carrier PCB and interdigitated silicon comb structure used for time-resolved evaluation. Red lines represent wire bonding between the PCB and 3 mm sample structure. The 50-ohm resistor is designed to match the impedance between the sample and PCB. (c) Optical microscopy image of the interdigitated silicon comb using a reflection geometry. (d) Time-resolved tine width measurement (along red line in inset) of the interdigitated comb sample using an excitation power of 0.5 W and four defocus heights (1.2 mm, 2.3 mm, 4.8 mm, 12 mm). (e) Power transmission measurements for the new RF compatible TEM holder compared to previous publications [30,31].

Through the imaging capabilities of the pulser we have further pushed our capabilities to conduct laser-free UEM experiments at high spatiotemporal resolutions. Specifically, our new RF compatible TEM holder enables substantial improvement in RF signal transmission over a 0-6 GHz frequency range [30,31]. Diverging from focus also disperses the range of momentum vectors in the electron beam at the image plane causing the apparent tine width fluctuation to amplify during peaks and valleys in RF excitation. The result is like other defocusing techniques that amplify contrast mechanisms (*i.e.*, Lorentz imaging) where larger defocus values cause a larger dispersion of the electron momenta during the beam-specimen interaction (see Fig. 6d). The

apparent deflection of the electrons becomes stronger causing the effective size fluctuation of the tines to increase. Observed breathing modes due to the electrostatic deflection can potentially be utilized to study other indirect dynamics such as spin-wave generation or propagation in spintronic devices. We expect that our advancements on the electron pulser will push the boundary of time-resolved dynamic elucidation to each of the techniques which have presented throughout this discussion.

4. SUMMARY AND CONCLUSIONS

In summary, we have demonstrated enhanced imaging capabilities using the electron pulser in a traditional TEM with a newly installed high-resolution polepiece at BNL to illustrate its performance in various microscopy techniques. Each technique utilizing a pulsed electron beam was compared to the continuous mode. In every technique, electron counts decrease by nearly 80%, even though physical measurements such as lattice spacings and spin contrast are retained. As a result, the immediate negative consequence for the user is longer acquisition times (inversely proportional to beam duty cycle) than a traditional microscope. Furthermore, the best results are yielded for the non-ultrahigh magnification techniques, as the influence of RF field sweeping is less noticeable. Clearly, the development of the electron pulser is still in its infancy and there are still improvements which can be made, but the current performance can capture structural features as small as 0.2 nm. Further, the electron beam coherency is retained better for features aligned parallel to the sweeping direction of the RF field. We have also built a new RF compatible TEM holder which can transmit over 40% more power to the sample during excitation which will enable more efficient probing of electronic, magnetic and structural dynamics.

ASSOCIATED CONTENT

Supporting Information

The Supporting Information includes additional details about the Materials and Methods, six Supplementary Figures of the procedures and explanations and one supplementary table of modulation and demodulation parameters.

Author Information

Corresponding Author

*Email: zhu@bnl.gov

ORCID

Yimei Zhu: 0000-0002-1638-7217

Spencer A. Reisbick: 0000-0002-7882-4152

M-G Han: 0000-0002-3736-3281

Chuhang Liu: 0000-0001-7162-4708

Eric Montgomery: 0000-0003-2486-5829

Chunguang Jing: 0000-0002-3333-1231

Yubin Zhao: 0000-0003-2327-8921

June W. Lau: 0000-0002-5233-4956

Jason J. Gorman: 0000-0003-2148-2312

Funding

This work was supported by the Materials Science and Engineering Divisions, Office of Basic Energy Sciences of the U.S. Department of Energy under Contract No. DESC0012704. The electron pulser was developed by Euclid through the DOE's SBIR grant under contract DE-SC0013121.

Notes

The authors declare no competing financial interest.

Acknowledgements

We thank JEOL engineers Robert Connor and Joseph Girgis for their time during installation week to optimize the emission parameters and alignment of the microscope.

REFERENCES

[1] P.E. Batson, N. Dellby, O.L. Krivanek, Sub-ångstrom resolution using aberration corrected electron optics, Nature. 418 (2002) 617–620. https://doi.org/10.1038/nature00972.

[2] R. Erni, M.D. Rossell, C. Kisielowski, U. Dahmen, Atomic-resolution imaging with a sub-50-pm electron probe, Phys. Rev. Lett. 102 (2009) 1–4. https://doi.org/10.1103/PhysRevLett.102.096101.

[3] A.R. Faruqi, Direct Electron Detectors for Electron Microscopy, Adv. Imaging Electron Phys. 145 (2007) 55–93. https://doi.org/10.1016/S1076-5670(06)45002-3.

[4] A.R. Faruqi, D.M. Cattermole, C. Raeburn, Direct electron detection methods in electron microscopy, Nucl. Instruments Methods Phys. Res. Sect. A Accel. Spectrometers, Detect. Assoc. Equip. 513 (2003) 317–321. https://doi.org/10.1016/j.nima.2003.08.055.

[5] T. Komoda, Study on the Structure of Evaporated Gold Particles by Means of a High Resolution Electron Microscope, Jpn. J. Appl. Phys. 7 (1968) 27–30. https://doi.org/10.1143/jjap.7.27.

[6] J.I. Goldstein, C.E. Lyman, D.B. Williams, The wavelength-dispersive spectrometer and its proposed use in the Analytical Electron Microscope, Ultramicroscopy. 28 (1989) 162–164. https://doi.org/10.1016/0304-3991(89)90289-1.

[7] L.A. Bendersky, F.W. Gayle, Electron Diffraction Using Transmission Electron Microscopy, J. Res. Natl. Inst. Stand. Technol. 106 (2001) 997–1012. https://doi.org/10.6028/jres.106.051.

[8] D.B. Williams, C.B. Carter, Transmission Electron Microscopy, 2nd ed., Springer Science, New York, 1996.

[9] A.R. Faruqi, G. McMullan, Direct imaging detectors for electron microscopy, Nucl. Instruments Methods Phys. Res. Sect. A Accel. Spectrometers, Detect. Assoc. Equip. 878 (2018) 180–190. https://doi.org/10.1016/j.nima.2017.07.037.

[10] C.M. O'Leary, C.S. Allen, C. Huang, J.S. Kim, E. Liberti, P.D. Nellist, A.I. Kirkland, Phase reconstruction using fast binary 4D STEM data, Appl. Phys. Lett. 116 (2020) 124101. https://doi.org/10.1063/1.5143213.

[11] I. MacLaren, T.A. MacGregor, C.S. Allen, A.I. Kirkland, Detectors-The ongoing revolution in scanning transmission electron microscopy and why this important to material characterization, APL Mater. 8 (2020) 110901. https://doi.org/10.1063/5.0026992.

[12] E.J. Vandenbussche, D.J. Flannigan, Reducing Radiation Damage in Soft Matter with Femtosecond-Timed Single-Electron Packets, Nano Lett. 19 (2019) 6687–6694. https://doi.org/10.1021/acs.nanolett.9b03074.

[13] R.M. Glaeser, K.A. Taylor, Radiation damage relative to transmission electron microscopy of biological specimens at low temperature: a review, J. Microsc. 112 (1978) 127–138. https://doi.org/10.1111/j.1365-2818.1978.tb01160.x.

[14] T. Wang, W. Lu, Q. Yang, S. Li, X. Yu, J. Qiu, X. Xu, S.F. Yu, In Situ Observation of Nucleation and Crystallization of a Single Nanoparticle in Transparent Media, J. Phys. Chem. C. 124 (2020) 15533–15540. https://doi.org/10.1021/acs.jpcc.0c03402.

[15] I. Akimoto, Y. Handa, K. Fukai, N. Naka, High carrier mobility in ultrapure diamond measured by time-resolved cyclotron resonance, Appl. Phys. Lett. 105 (2014) 032102. https://doi.org/10.1063/1.4891039.

[16] U. Bovensiepen, P.S. Kirchmann, Elementary relaxation processes investigated by femtosecond photoelectron spectroscopy of two-dimensional materials, Laser Photonics Rev. 6 (2012) 589–606. https://doi.org/10.1002/lpor.201000035.

[17] F.U. Stein, L. Bocklage, M. Weigand, G. Meier, Time-resolved imaging of nonlinear magnetic domain-wall dynamics in ferromagnetic nanowires, Sci. Rep. 3 (2013) 7–10. https://doi.org/10.1038/srep01737.

[18] J. Vogel, W. Kuch, M. Bonfim, J. Camarero, Y. Pennec, F. Offi, K. Fukumoto, J. Kirschner, A. Fontaine, S. Pizzini, Time-resolved magnetic domain imaging by x-ray photoemission electron microscopy, Appl. Phys. Lett. 82 (2003) 2299–2301. https://doi.org/10.1063/1.1564876.

[19] D.P. DiVincenzo, D. Loss, Coupled quantum dots as quantum gates, Phys. Rev. B - Condens. Matter Mater. Phys. 59 (1999) 2070–2078. https://doi.org/10.1103/PhysRevB.59.2070.

[20] N.M. Linke, D. Maslov, M. Roetteler, S. Debnath, C. Figgatt, K.A. Landsman, K. Wright,

C. Monroe, Experimental comparison of two quantum computing architectures, Proc. Natl. Acad. Sci. U. S. A. 114 (2017) 3305–3310. https://doi.org/10.1073/pnas.1618020114.

[21] A. Houshang, R. Khymyn, H. Fulara, A. Gangwar, M. Haidar, S.R. Etesami, R. Ferreira, P.P. Freitas, M. Dvornik, R.K. Dumas, J. Åkerman, Spin transfer torque driven higher-order propagating spin waves in nano-contact magnetic tunnel junctions, Nat. Commun. 9 (2018) 1–6. https://doi.org/10.1038/s41467-018-06589-0.

[22] T. Schneider, A.A. Serga, B. Leven, B. Hillebrands, R.L. Stamps, M.P. Kostylev, Realization of spin-wave logic gates, Appl. Phys. Lett. 92 (2008) 022505. https://doi.org/10.1063/1.2834714.

[23] Y. Kajiwara, K. Harii, S. Takahashi, J. Ohe, K. Uchida, M. Mizuguchi, H. Umezawa, H. Kawai, K. Ando, K. Takanashi, S. Maekawa, E. Saitoh, Transmission of electrical signals by spin-wave interconversion in a magnetic insulator, Nature. 464 (2010) 262–266. https://doi.org/10.1038/nature08876.

[24] D.A. Plemmons, D.J. Flannigan, Ultrafast electron microscopy: Instrument response from the single-electron to high bunch-charge regimes, Chem. Phys. Lett. 683 (2017) 186–192. https://doi.org/10.1016/j.cplett.2017.01.055.

[25] Y.J. Kim, H. Jung, S.W. Han, O.H. Kwon, Ultrafast Electron Microscopy Visualizes Acoustic Vibrations of Plasmonic Nanorods at the Interfaces, Matter. 1 (2019) 481–495. https://doi.org/10.1016/j.matt.2019.03.004.

[26] A. Feist, N. Bach, N. Rubiano da Silva, T. Danz, M. Möller, K.E. Priebe, T. Domröse, J.G. Gatzmann, S. Rost, J. Schauss, S. Strauch, R. Bormann, M. Sivis, S. Schäfer, C. Ropers, Ultrafast transmission electron microscopy using a laser-driven field emitter: Femtosecond resolution with a high coherence electron beam, Ultramicroscopy. 176 (2017) 63–73.

https://doi.org/10.1016/j.ultramic.2016.12.005.

[27] L. Zhang, J.P. Hoogenboom, B. Cook, P. Kruit, Photoemission sources and beam blankers for ultrafast electron microscopy, Struct. Dyn. 6 (2019) 051501. https://doi.org/10.1063/1.5117058.

[28] W. Verhoeven, J.F.M. van Rens, E.R. Kieft, P.H.A. Mutsaers, O.J. Luiten, High quality ultrafast transmission electron microscopy using resonant microwave cavities, Ultramicroscopy. 188 (2018) 85–89. https://doi.org/10.1016/j.ultramic.2018.03.012.

[29] M. Möller, J.H. Gaida, S. Schäfer, C. Ropers, Few-nm tracking of current-driven magnetic vortex orbits using ultrafast Lorentz microscopy, Commun. Phys. 3 (2020) 1–7. https://doi.org/10.1038/s42005-020-0301-y.

[30] J.W. Lau, K.B. Schliep, M.B. Katz, V.J. Gokhale, J.J. Gorman, C. Jing, A. Liu, Y. Zhao, E. Montgomery, H. Choe, W. Rush, A. Kanareykin, X. Fu, Y. Zhu, Laser-free GHz stroboscopic transmission electron microscope: Components, system integration, and practical considerations for pump-probe measurements, Rev. Sci. Instrum. 91 (2020) 021301. https://doi.org/10.1063/1.5131758.

[31] X. Fu, E. Wang, Y. Zhao, A. Liu, E. Montgomery, V.J. Gokhale, J.J. Gorman, C. Jing, J.W. Lau, Y. Zhu, Direct visualization of electromagnetic wave dynamics by laser-free ultrafast electron microscopy, Sci. Adv. 6 (2020) eabc3456. https://doi.org/10.1126/sciadv.abc3456.

[32] C. Jing, Y. Zhu, A. Liu, K. Schliep, X. Fu, Y. Zhao, E. Montgomery, W. Rush, A. Kanareykin, M. Katz, J. Lau, Tunable electron beam pulser for picoseconds stroboscopic microscopy in transmission electron microscopes, Ultramicroscopy. 207 (2019) 112829. https://doi.org/10.1016/j.ultramic.2019.112829.

[33] R.W. Vook, M.A. Otooni, Lattice parameter of thin gold films, J. Appl. Phys. 39 (1968)

2471–2472. https://doi.org/10.1063/1.1656581.

[34] A. Gentils, J.N. Chapman, G. Xiong, R.P. Cowburn, Variation of domain-wall structures and magnetization ripple spectra in permalloy films with controlled uniaxial anisotropy, J. Appl. Phys. 98 (2005) 053905. https://doi.org/10.1063/1.2033152.

[35] M. De Graef, Recent advances in quantitative Lorentz microscopy, INTERMAG Eur. 2002 - IEEE Int. Magn. Conf. (2002) 1–22. https://doi.org/10.1109/INTMAG.2002.1001118.

[36] V. V. Volkov, Y. Zhu, Lorentz phase microscopy of magnetic materials, Ultramicroscopy. 98 (2004) 271–281. https://doi.org/10.1016/j.ultramic.2003.08.026.

[37] C. Liu, J. Chen, T. Liu, F. Heimbach, H. Yu, Y. Xiao, J. Hu, M. Liu, H. Chang, T. Stueckler, S. Tu, Y. Zhang, Y. Zhang, P. Gao, Z. Liao, D. Yu, K. Xia, N. Lei, W. Zhao, M. Wu, Long-distance propagation of short-wavelength spin waves, Nat. Commun. 9 (2018) 4–11. https://doi.org/10.1038/s41467-018-03199-8.

[38] S.A. Reisbick, Y. Zhang, D.J. Flannigan, Influence of Discrete Defects on Observed Acoustic-Phonon Dynamics in Layered Materials Probed with Ultrafast Electron Microscopy, J. Phys. Chem. A. 124 (2020) 1877–1884. https://doi.org/10.1021/acs.jpca.9b12026.

[39] D.R. Cremons, D.X. Du, D.J. Flannigan, Picosecond phase-velocity dispersion of hypersonic phonons imaged with ultrafast electron microscopy, Phys. Rev. Mater. 1 (2017) 073801. https://doi.org/10.1103/PhysRevMaterials.1.073801.

[40] A. Feist, N. Rubiano Da Silva, W. Liang, C. Ropers, S. Schäfer, Nanoscale diffractive probing of strain dynamics in ultrafast transmission electron microscopy, Struct. Dyn. 5 (2018). https://doi.org/10.1063/1.5009822.

[41] A.J. McKenna, J.K. Eliason, D.J. Flannigan, Spatiotemporal Evolution of Coherent Elastic

Strain Waves in a Single MoS2 Flake, Nano Lett. 17 (2017) 3952–3958. https://doi.org/10.1021/acs.nanolett.7b01565.

[42] D.R. Cremons, D.A. Plemmons, D.J. Flannigan, Defect-mediated phonon dynamics in TaS2 and WSe2, Struct. Dyn. 4 (2017) 044019. https://doi.org/10.1063/1.4982817.

[43] A. Yurtsever, A.H. Zewail, Kikuchi ultrafast nanodiffraction in four-dimensional electron microscopy, Proc. Natl. Acad. Sci. U. S. A. 108 (2011) 3152–3156. https://doi.org/10.1073/pnas.1018733108.

[44] O.H. Kwon, B. Barwick, H.S. Park, J.S. Baskin, A.H. Zewail, Nanoscale mechanical drumming visualized by 4D electron microscopy, Nano Lett. 8 (2008) 3557–3562. https://doi.org/10.1021/nl8029866.

[45] X. Fu, F. Barantani, S. Gargiulo, I. Madan, G. Berruto, T. LaGrange, L. Jin, J. Wu, G.M. Vanacore, F. Carbone, Y. Zhu, Nanoscale-femtosecond dielectric response of Mott insulators captured by two-color near-field ultrafast electron microscopy, Nat. Commun. 11 (2020) 1–11. https://doi.org/10.1038/s41467-020-19636-6.

[46] S.K. Sinha, A. Khammari, M. Picher, F. Roulland, N. Viart, T. LaGrange, F. Banhart, Nanosecond electron pulses in the analytical electron microscopy of a fast irreversible chemical reaction, Nat. Commun. 10 (2019) 3648. https://doi.org/10.1038/s41467-019-11669-w.

[47] M.S. Grinolds, V.A. Lobastov, J. Weissenrieder, A.H. Zewail, Four-dimensional ultrafast electron microscopy of phase transitions, Proc. Natl. Acad. Sci. U. S. A. 103 (2006) 18427–18431. https://doi.org/10.1073/pnas.0609233103.

[48] J.W. Lau, M. Beleggia, Y. Zhu, Common reversal mechanisms and correlation between transient domain states and field sweep rate in patterned Permalloy structures, J. Appl. Phys.

102 (2007) 1–6. https://doi.org/10.1063/1.2769779.

[49] J.W. Lau, M. Beleggia, M.A. Schofield, G.F. Neumark, Y. Zhu, Direct correlation of reversal rate dynamics to domain configurations in micron-sized permalloy elements, J. Appl. Phys. 97 (2005) 22–24. https://doi.org/10.1063/1.1851731.

[50] T.E. Gureyev, A. Roberts, K.A. Nugent, Partially coherent fields, the transport-of-intensity equation, and phase uniqueness, J. Opt. Soc. Am. A. 12 (1995) 1942. https://doi.org/10.1364/josaa.12.001942.

[51] M. Beleggia, M.A. Schofield, V. V. Volkov, Y. Zhu, On the transport of intensity technique for phase retrieval, Ultramicroscopy. 102 (2004) 37–49. https://doi.org/10.1016/j.ultramic.2004.08.004.

[52] A. Kohn, A. Habibi, M. Mayo, Experimental evaluation of the "transport-of-intensity" equation for magnetic phase reconstruction in Lorentz transmission electron microscopy, Ultramicroscopy. 160 (2016) 44–56. https://doi.org/10.1016/j.ultramic.2015.09.011.

[53] P.K. Olshin, G. Bongiovanni, M. Drabbels, U.J. Lorenz, Atomic-Resolution Imaging of Fast Nanoscale Dynamics with Bright Microsecond Electron Pulses, Nano Lett. 21 (2021) 612–618. https://doi.org/10.1021/acs.nanolett.0c04184.

[54] F. Houdellier, A. Masseboeuf, M. Monthioux, M.J. Hÿtch, New carbon cone nanotip for use in a highly coherent cold field emission electron microscope, Carbon N. Y. 50 (2012) 2037–2044. https://doi.org/10.1016/j.carbon.2012.01.023.

[55] M.R. Scheinfein, W. Qian, J.C.H. Spence, Aberrations of emission cathodes: Nanometer diameter field-emission electron sources, J. Appl. Phys. 73 (1993) 2057–2068. https://doi.org/10.1063/1.353151.

[56] J.C.H. Spence, W. Qian, M.P. Silverman, Electron source brightness and degeneracy from

Fresnel fringes in field emission point projection microscopy, J. Vac. Sci. Technol. A Vacuum, Surfaces, Film. 12 (1994) 542–547. https://doi.org/10.1116/1.579166.

[i] Certain commercial equipment, instruments, or materials are identified in this presentation to specify the experimental procedure adequately. Such identification is not intended to imply recommendation or endorsement by the National Institute of Standards and Technology, nor is it intended to imply that the materials or equipment identified are necessarily the best available for the purpose.